A&A 631, A34 (2019)
https://doi.org/10.1051/0004-6361/201935718
© ESO 2019

Astronomy & Astrophysics

The GAPS Programme with HARPS-N at TNG

XIX. Atmospheric Rossiter-McLaughlin effect and improved parameters of KELT-9b[⋆,⋆⋆]

F. Borsa[1], M. Rainer[2], A. S. Bonomo[3], D. Barbato[4,3], L. Fossati[5], L. Malavolta[6], V. Nascimbeni[7], A. F. Lanza[6], M. Esposito[8], L. Affer[9], G. Andreuzzi[10,23], S. Benatti[9], K. Biazzo[6], A. Bignamini[11], M. Brogi[12,13,3], I. Carleo[14], R. Claudi[7], R. Cosentino[10], E. Covino[15], M. Damasso[3], S. Desidera[7], A. Garrido Rubio[9,16], P. Giacobbe[3], E. González-Álvarez[17], A. Harutyunyan[10], C. Knapic[11], G. Leto[6], R. Ligi[1], A. Maggio[9], J. Maldonado[9], L. Mancini[18,19,3], A. F. M. Fiorenzano[10], S. Masiero[24], G. Micela[9], E. Molinari[20], I. Pagano[6], M. Pedani[10], G. Piotto[21], L. Pino[22], E. Poretti[1,10], G. Scandariato[6], R. Smareglia[11], and A. Sozzetti[3]

(Affiliations can be found after the references)

Received 17 April 2019 / Accepted 23 July 2019

ABSTRACT

Aims. In the framework of the GAPS project, we observed the planet-hosting star KELT-9 (A-type star, $v \sin i \sim 110$ km s^{-1}) with the HARPS-N spectrograph at the Telescopio Nazionale *Galileo*. In this work we analyse the spectra and the extracted radial velocities to constrain the physical parameters of the system and to detect the planetary atmosphere of KELT-9b.

Methods. We extracted the mean stellar line profiles from the high-resolution optical spectra via an analysis based on the least-squares deconvolution technique. Then we computed the stellar radial velocities with a method optimised for fast rotators by fitting the mean stellar line profile with a purely rotational profile instead of using a Gaussian function.

Results. The new spectra and analysis led us to update the orbital and physical parameters of the system, improving in particular the value of the planetary mass to $M_{\rm p} = 2.88 \pm 0.35\, M_{\rm Jup}$. We discovered an anomalous in-transit radial velocity deviation from the theoretical Rossiter-McLaughlin effect solution, calculated from the projected spin-orbit angle $\lambda = -85.78 \pm 0.46$ degrees measured with Doppler tomography. We prove that this deviation is caused by the planetary atmosphere of KELT-9b, thus we call this effect Atmospheric Rossiter-McLaughlin effect. By analysing the magnitude of the radial velocity anomaly, we obtained information on the extension of the planetary atmosphere as weighted by the model used to retrieve the stellar mean line profiles, which is up to $1.22 \pm 0.02\, R_{\rm p}$.

Conclusions. The Atmospheric Rossiter-McLaughlin effect will be observable for other exoplanets whose atmosphere has non-negligible correlation with the stellar mask used to retrieve the radial velocities, in particular ultra-hot Jupiters with iron in their atmospheres. The duration and amplitude of the effect will depend not only on the extension of the atmosphere, but also on the in-transit planetary radial velocities and on the projected rotational velocity of the parent star.

Key words. planetary systems – techniques: spectroscopic – techniques: radial velocities – planets and satellites: atmospheres – stars: individual: KELT-9

1. Introduction

During the last two decades we have witnessed a huge expansion in exoplanet science. By analysing demographic trends in exoplanet populations, many surprises and questions have emerged. This means that a larger observed sample (and thus more extensive surveys) is crucial in order to have a comprehensive view of exoplanetst (e.g. Winn & Fabrycky 2015). We are finding planetary architectures that are completely different from theoretical predictions, including extreme planetary systems. This diversity of exoplanetary systems reflects an incredible heterogeneity of exoplanetary atmospheres (e.g. Sing et al. 2016). Thanks to technological and methodological progress, we are increasing our ability to probe the atmospheric composition of other planets with the help of many different techniques (e.g. Deming & Seager 2017). In this context, it is necessary to have small uncertainties on the parameters of the whole star–planet system to deeply characterise the physical and chemical processes of exoplanetary climates and interiors (Madhusudhan et al. 2016).

KELT-9 (Gaudi et al. 2017) is one of the most striking examples of extreme systems: orbiting an A-type star with an effective temperature of ∼10 000 K with a period of 1.48 days, the ultra-hot Jupiter KELT-9b reaches dayside equilibrium temperatures comparable to those of late K-type stars. At these high temperatures the atmospheric conditions are extreme (Kitzmann et al. 2018; Lothringer et al. 2018), and it has been possible to recover some properties that were unexpected for planets.

Yan & Henning (2018) detected hydrogen Balmer (Hα) absorption in the planetary atmosphere, extending up to the typical location of the thermosphere, indicating the presence of escaping excited hydrogen. They derived a planetary mass-loss rate of about 10^{12} g s^{-1} from the hydrogen atmospheric

⋆ Full Table 2 is only available at the CDS via anonymous ftp to cdsarc.u-strasbg.fr (130.79.128.5) or via http://cdsarc.u-strasbg.fr/viz-bin/cat/J/A+A/631/A34

⋆⋆ Based on observations made with the Italian Telescopio Nazionale *Galileo* (TNG) operated on the island of La Palma by the Fundacion Galileo Galilei of the INAF at the Spanish Observatorio Roque de los Muchachos of the IAC in the frame of the program Global Architecture of the Planetary Systems (GAPS).

density extracted from the data, hence ignoring the effect of the heating provided by the stellar high-energy emission (i.e. in the extreme ultraviolet, XUV), which led them to suggest that the mass-loss rate may be even higher. However, as shown by Fossati et al. (2018), this estimate is expected to be correct because early A-type stars, such as KELT-9, do not possess significant XUV emission, which would further increase mass loss. This can also explain why the atmosphere of KELT-9b has not completely escaped without requiring a short-lived evolutionary phase (Fossati et al. 2018). Hoeijmakers et al. (2018) have found evidence of neutral and singly ionised iron and singly ionised titanium in the planetary atmosphere, while Cauley et al. (2019) have published the first detection of magnesium in an exoplanet and the presence of a dynamic atmosphere.

In this work, we update the KELT-9 system orbital and physical parameters and show that the planetary atmosphere can be detected through residual line profiles and in-transit radial velocity (RV) measurements. We find an in-transit RV deviation ascribable not only to the classical Rossiter-McLaughlin (RML) effect, which is caused by the Doppler shadow of the planet on the stellar mean line profile, but also by another effect arising from the planetary atmosphere detected thanks to the match with the stellar mask used to recover the stellar mean line profile.

2. Data sample

In the framework of the GAPS project (Covino et al. 2013), we observed KELT-9 during four transits of KELT-9b and twice out of transit with the HARPS-N and GIANO-B high-resolution spectrographs, mounted at the Telescopio Nazionale *Galileo*. We used the GIARPS configuration (Claudi et al. 2017), that allowed us to observe simultaneously with the two spectrographs, obtaining high-resolution spectra in the wavelength range ~390–690 and ~940–2420 nm. In this work, we analyse only the HARPS-N spectra. The GIANO-B spectra will be presented in a future work, aimed at an in-depth atmospheric characterisation of the planet.

The transit of KELT-9b lasts ~4 h. The first transit observations were taken with low-cadence sampling with long exposures (600 s), while for the other three transits we used a higher cadence (300 s exposures). Fiber A of the spectrograph was centred on the target, and at the same time fiber B was monitoring the sky. A log of the observations is given in Table 1. During the observations of transits 1 and 2 (and during the out-of-transit pointings) there was a problem with the atmospheric dispersion correctors (ADC) of the telescope, which remained stuck in the same position for the duration of each observing block and was updated only after re-pointing the object. This caused a significant loss of flux, in particular in the blue part of the spectrum. We note that our final results are valid even when considering only transits 3 and 4, and thus are not affected by the ADC problems.

The data were reduced with the version 3.7 of the HARPS-N Data Reduction Software (DRS) pipeline using the YABI interface with custom parameters (e.g. Borsa et al. 2015), in particular enlarging the cross-correlation function (CCF) width because of the large $v \sin i$ of the star. However, due to the ADC problems (and possibly also to the spectral type of the star, which does not have a proper colour correction template), we could not trust the given CCFs, which suffered from a clearly imperfect continuum normalisation. We thus started our analysis from the reduced one-dimensional spectra after they had been properly normalised. We collected a total of 373 spectra, 226 bracketing four transits and 147 at other orbital phases. We excluded from our final transit RV analysis all the data with a signal-to-noise ratio $(S/N) < 70$ (as measured in order 46) or taken at airmass >1.7, thus discarding 11 of the 226 exposures collected. Adopting the transit ephemerides from Gaudi et al. (2017), we analysed 148 in-transit and 67 out-of-transit exposures.

Table 1. KELT-9b HARPS-N observations log.

Transit number	Night	Exposure time	$N_{\rm obs}$	$S/N_{\rm ave}$
1	10 Jun 2018	600 s	36	156
2	23 Jul 2018	300 s	68	104
3	01 Sep 2018	300 s	58	118
4	04 Sep 2018	300 s	64	102
Out of transit	08 Jul 2018	300 s	58	78
Out of transit	22 Jul 2018	300 s	89	135

3. Radial velocity extraction

The extraction of RVs from echelle spectra is usually done with a Gaussian fit on the CCFs of the different orders, properly combined with a weighted average (Baranne et al. 1996; Pepe et al. 2002). For fast rotators, this procedure leads to large uncertainties on the derived RV value as the rotational broadening is too large to ensure sufficient precision. As we could not exploit the CCFs from the DRS, we extracted the RVs with a custom-made routine. We computed the stellar mean line profiles using the least-squares deconvolution (LSD) software (Donati et al. 1997). This software performs a deconvolution via a least-squares analysis of the normalised spectra with a theoretical line mask extracted from the Vienna Atomic Line Database (VALD; Piskunov et al. 1995). We used a stellar mask with $T_{\rm eff} = 10\,000$ K, $\log g = 4.0$, solar metallicity. We accurately re-normalised the spectra and converted them to the required format, working only on the wavelength regions 4415–4805 Å, 4915–5285 Å, 5365–5870 Å, 6050–6265 Å, and 6335–6450 Å; that is, we cut the blue orders where the S/N was very low due to the instrument efficiency (and the ADC problems), the Balmer lines, and the regions where most of the telluric lines are found.

To estimate the RVs, instead of using a Gaussian fit, we preferred to model the LSD lines with a rotational profile, using the formula in Eq. (1) (Gray 2008):

$$f(x) = 1 - 2a(1-\mu)\sqrt{1-\left(\frac{x-x_0}{x_l}\right)^2} + \frac{0.5\pi\mu\left[1-\left(\frac{x-x_0}{x_l}\right)^2\right]}{\pi x_l\left(1-\frac{\mu}{3}\right)}. \quad (1)$$

Here a is the depth of the profile, x the Doppler velocity, x_0 the centre (i.e. the RV value), x_l the $v \sin i$ of the star, μ the linear limb darkening (LD) coefficient. The theoretical linear LD coefficient, calculated using the code `LDTK` (which generates custom LD coefficients using a library of `PHOENIX`-generated specific intensity spectra; Parviainen & Aigrain 2015; Husser et al. 2013) for the same wavelength range used for the RV extraction and with our stellar parameters (Sect. 4) is $\mu = 0.47$. However, here we decided to adopt the value $\mu = 0.6$ because it minimises the RV residuals in the orbital fit (Sect. 4). This also reflects the ADC problems encountered (see Sect. 2), which strongly reduced the flux at blue wavelengths, and introduced a strong (and not quantifiable) bias in the flux distribution along the wavelength range.

Figure 1 shows an example of a mean line profile. It is evident that the rotational profile is by far more suitable than a

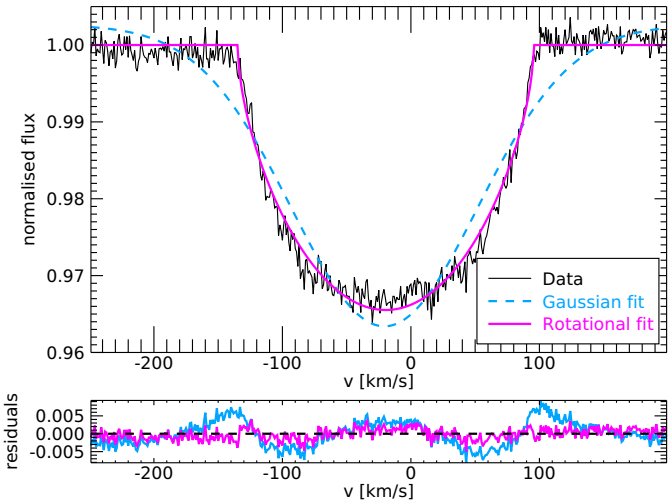

Fig. 1. Example of an out-of-transit stellar mean line profile of KELT-9. Also shown are the Gaussian (cyan dashed line) and rotational profile (magenta line) fits.

Table 2. HARPS-N RV observations of KELT-9.

Time [BJD-2 450 000]	RV [km s^{-1}]	RV error [km s^{-1}]
8280.46931	−19.565	0.295
8280.47643	−19.804	0.313
8280.48363	−19.663	0.263
8280.49091	−19.829	0.314
...	...	...

Notes. This table is available in its entirety at the CDS.

Gaussian function for fitting the line profile of fast rotators. A similar choice for extracting the RVs was also done by Anderson et al. (2018) and Johnson et al. (2018), among others. The extracted RVs for our KELT-9 HARPS-N observations are listed in Table 2.

We also derived the $v \sin i$ of the star from the rotational broadening fit (x_l parameter in Eq. (1)). Our result is $v \sin i = 111.8 \pm 1.0$ km s^{-1}, taken as the average value calculated on the out-of-transit mean line profiles with the relative standard deviation. We checked this value using the Fourier transform method on the line profiles (Gray 1976; Reiners & Schmitt 2002). The position of the first two zeros of the Fourier transform of a line profile is directly related to the $v \sin i$ when the rotational broadening is the largest broadening effect. This method yields a value of 110.0 ± 3.0 km s^{-1}, which is consistent with our $v \sin i$ measurement.

4. Updated parameters of the planetary system

We estimated the stellar atmospheric parameters by comparing the average of all collected HARPS-N spectra put in the stellar restframe with synthetic ones. In particular, we employed spectral synthesis with the SYNTH3 code (Kochukhov 2007) and the tools described by Fossati et al. (2007) to measure the abundance of FeI and FeII from 21 and 30 lines, respectively, for values of the effective temperature ($T_{\rm eff}$) ranging between 9000 and 10 200 K and surface gravity ($\log g$) ranging between 3.9 and 4.3. We then derived $T_{\rm eff}$ by imposing excitation equilibrium and $\log g$ by imposing ionisation equilibrium. We computed stellar atmosphere models using LLmodels

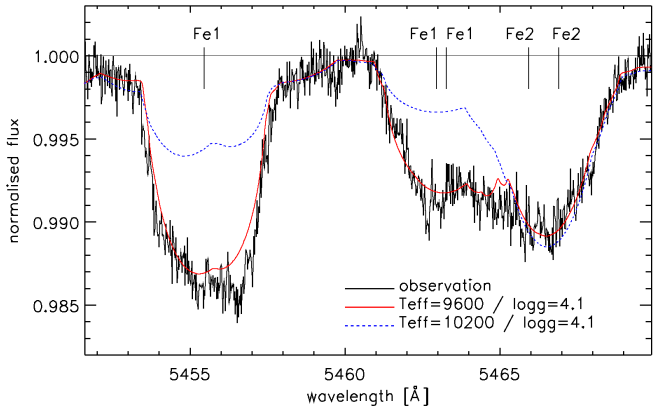

Fig. 2. Comparison of the average HARPS-N spectrum (black solid line), a synthetic spectrum obtained with the parameters derived from our analysis (red solid line), and a synthetic spectrum computed with the parameters of Gaudi et al. (2017, blue dashed line).

(Shulyak et al. 2004), which was developed specifically to study the atmospheres of A-type stars. Prior to proceeding with the line fits, we measured the stellar $v \sin i$ by fitting the profiles of several weakly blended or unblended lines obtaining a value of 108 ± 2 km s^{-1}, in agreement with our other estimates. The broad line profiles did not allow a direct measurement of the microturbulence velocity ($\upsilon_{\rm mic}$), hence we assumed it to be equal to 1 km s^{-1}, which has been shown to be an adequate value for early A-type stars (e.g. Fossati et al. 2009). We finally obtained $T_{\rm eff} = 9600 \pm 400$ K and $\log g = 4.1 \pm 0.3$ cm s^{-2}. The wings of hydrogen Balmer lines are best suited to derive $T_{\rm eff}$ and $\log g$ of A-type stars, particularly above 8500 K (e.g. Fossati et al. 2009), but low-frequency waves in the spectra did not enable us to perform an acceptable normalisation of these broad features. With the derived atmospheric parameters, we measured an iron abundance [Fe/H] = $+0.14 \pm 0.3$ dex.

The value of $T_{\rm eff}$ we obtained from the HARPS-N spectra is about 600 K lower than that found by Gaudi et al. (2017), but both values actually agree within 1σ given the large uncertainties of ~400 K. Figure 2 shows a small portion of the average HARPS-N spectrum in comparison to synthetic spectra computed with the parameters given by Gaudi et al. (2017) and derived from our analysis: our parameters better fit the observed spectrum.

Since the KELT-9 parallax provided by the *Gaia* second Data Release (DR2, Gaia Collaboration 2018), that is $\pi = 4.862 \pm 0.037$ mas, is significantly more precise than that used in Gaudi et al. (2017), we also re-determined the stellar parameters by fitting the spectral energy distribution (SED) and using the MIST evolutionary tracks (Dotter 2016) through the ExofastV2 code (Eastman 2017). We first corrected π for the systematic offset of -82 ± 33 μas in the *Gaia* DR2 parallaxes reported in Stassun & Torres (2018), then we used the same magnitudes as provided in Table 5 of Gaudi et al. (2017) and modified the ExofastV2 code to include the stellar fluxes from the Ultraviolet Sky Survey Telescope. The stellar parameters are simultaneously constrained by the SED and the MIST isochrones, imposing Gaussian priors on $T_{\rm eff}$ and [Fe/H] from our updated stellar atmospheric parameters. The SED primarily constrains the stellar radius and temperature, and a penalty for straying from the MIST evolutionary tracks ensures that the resulting star is physical. The derived stellar parameters are shown in Table 3 and the mass, radius, and age agree with those of Gaudi et al. (2017) within 1σ.

Table 3. Properties of the KELT-9 planetary system.

Stellar IDs		
HD 195689		
TYC 3157-638-1		
2MASS J20312634+3956196		
Stellar parameters		Source
Star mass $M_\star$ [$M_\odot$]	2.32 ± 0.16	This work
Star radius $R_\star$ [$R_\odot$]	2.418 ± 0.058	This work
Stellar luminosity $L_\star$ [$L_\odot$]	$38.9^{+4.3}_{-3.2}$	This work
Stellar density ρ_* [g cm^{-3}]	0.231 ± 0.025	This work
Effective temperature $T_{\rm eff}$ [K]	9600 ± 400	This work [(a)]
Derived effective temperature $T_{\rm eff}$ [K]	9270^{+240}_{-180}	This work [(b)]
Surface gravity $\log g$ [cgs]	4.1 ± 0.3	This work [(a)]
Derived surface gravity $\log g$ [cgs]	$4.037^{+0.038}_{-0.040}$	This work [(b)]
Metallicity [Fe/H] [dex]	0.14 ± 0.30	This work [(a)]
Derived metallicity [Fe/H] [dex]	$0.07^{+0.20}_{-0.23}$	This work [(b)]
Age t [Gyr]	$0.45^{+0.14}_{-0.13}$	This work
HARPS-N systemic velocity $V_{\rm r,HN}$ [km s^{-1}]	-19.819 ± 0.024	This work
TRES radial-velocity zero point $V_{\rm r,TRES}$ [km s^{-1}]	0.391 ± 0.057	This work
HARPS-N radial-velocity jitter $s_{\rm j,HN}$ [km s^{-1}]	0.075 ± 0.048	This work
TRES radial-velocity jitter $s_{\rm j,TRES}$ [km s^{-1}]	0.138 ± 0.074	This work
Gaia DR2 parallax π [mas]	4.944 ± 0.050	This work
Interstellar extinction A_V	$0.106^{+0.077}_{-0.064}$	This work
Stellar distance d [pc]	202.3 ± 2.0	This work
Transit and orbital parameters		Source
Orbital period P [d]	1.4811235 ± 0.0000011	Gaudi et al. (2017)
Transit epoch T_0[BJD$_{\rm TDB}$ − 2 450 000]	7095.68572 ± 0.00014	Gaudi et al. (2017)
Radius ratio $R_{\rm p}/R_*$	0.08228 ± 0.00043	Gaudi et al. (2017)
Inclination i [deg]	86.79 ± 0.25	Gaudi et al. (2017)
Orbital eccentricity e	0 (fixed)	Gaudi et al. (2017)
Radial velocity semi-amplitude K [m s^{-1}]	293 ± 32	This work
Planetary parameters		Source
Planet mass $M_{\rm p}$ [$M_{\rm Jup}$]	2.88 ± 0.35	This work
Planet radius $R_{\rm p}$ [$R_{\rm Jup}$]	1.936 ± 0.047	This work
Planet density $\rho_{\rm p}$ [g cm^{-3}]	$0.491^{+0.072}_{-0.066}$	This work
Planet surface gravity $\log g_{\rm p}$ [cgs]	$3.279^{+0.053}_{-0.058}$	This work
Orbital semi-major axis a [AU]	0.03368 ± 0.00078	This work
Equilibrium temperature $T_{\rm eq}$ [K] [(c)]	3921^{+182}_{-174}	This work

Notes. [(a)]From the analysis of HARPS-N spectra. [(b)]From SED fitting and MIST evolutionary tracks by using the ExofastV2 tool and imposing Gaussian priors on $T_{\rm eff}$ and [Fe/H] from the spectral analysis. [(c)]Black-body equilibrium temperature assuming a null Bond albedo and uniform heat redistribution to the night-side.

We modelled the TRES RVs from literature (Gaudi et al. 2017) and our HARPS-N RVs with a Keplerian circular orbit in a Bayesian framework by employing a differential evolution Markov chain Monte Carlo (DE-MCMC) technique (Ter Braak 2006; Eastman et al. 2013). The circular orbit is justified by (i) the strong constraint on the eccentricity from the observations of the secondary eclipse, that is $e < 0.015$ (Gaudi et al. 2017, Extended Data Table 3), and (ii) the expected circularisation of the orbit for star–planet tidal interactions, given that the circularisation timescale of ~2–5 Myr for a modified tidal quality factor $Q'_{\rm p} \sim 10^6$ is considerably shorter than the system age (~450 Myr). We fitted seven free parameters: the mid-transit time $T_{\rm c}$, the orbital period P, the RV semi-amplitude K, and two RV zero points ($V_{\rm r,HN}$ and $V_{\rm r,TRES}$) and jitter terms ($s_{\rm j,HN}$ and $s_{\rm j,TRES}$) for the two spectrographs HARPS-N and TRES, respectively. We imposed Gaussian priors on $T_{\rm c}$ and P from the orbital ephemeris in Gaudi et al. (2017) and uninformative priors on all the other parameters. We ran 14 DE-MCMC chains by adopting the same likelihood function and prescriptions as in Bonomo et al. (2017). The medians and the 15.86 and 84.14% quantiles of the posterior distributions were taken as the best values and 1σ uncertainties, and are listed in Table 3. The Keplerian best fit is shown in Fig. 3. Unlike Yan & Henning (2018) who estimated the planetary RVs from the planetary atmospheric track

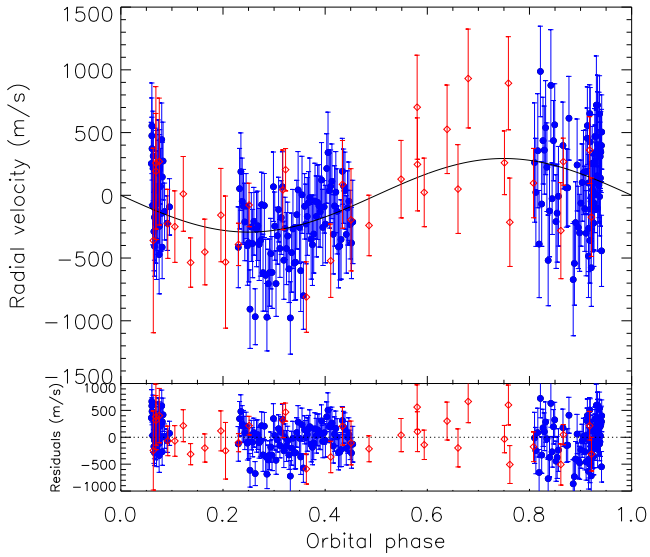

Fig. 3. HARPS-N (blue circles) and TRES (red diamonds) out-of-transit radial velocities of KELT-9 as a function of the orbital phase along with the best Keplerian model (black solid line). The mid-transit corresponds to phases equal to zero or one.

(using Hα), we did not because in our data we detected possible hints of atmospheric dynamics that could cause a deviation from the planetary Keplerian motion; this effect will be analysed in another paper.

Finally, we combined the posterior distributions of the stellar, orbital, and transit parameters (the last from Gaudi et al. 2017) to redetermine the planetary parameters (see Table 3). In summary, we find a radius $R_p = 1.936 \pm 0.047\, R_{Jup}$, a mass $M_p = 2.88 \pm 0.35\, M_{Jup}$, and thus a density $\rho_p = 0.491^{+0.072}_{-0.066}$ g cm^{-3} for KELT-9b. These planetary parameters are certainly consistent with those that were previously determined by Gaudi et al. (2017), but are more precise. In particular, the significance of our planetary mass measurement increased from 3.4σ to 8.2σ, and that of the planetary density from 3.5σ to 7.4σ, which is a remarkable improvement given the large RV uncertainties due to the high $v \sin i$ of the star.

5. In-transit RVs: the Atmospheric Rossiter-McLaughlin effect

For each transit sequence we subtracted the mean in-transit RV from each RV to avoid any possible offset caused by instabilities and long-term trends in the orbital solution, and then averaged the RVs of the four transits in bins of 0.005 in phase. The RV time series of each single transit and their average are shown in Fig. 4.

For KELT-9b, by using the technique of line-profile tomography (e.g. Collier Cameron et al. 2010) the projected orbital plane inclination with respect to the stellar rotational axis was found to be $\lambda = -84.8 \pm 1.4$ degrees (Gaudi et al. 2017). By applying their same Doppler shadow model to our data, we updated this value to $\lambda = -85.78 \pm 0.46$ degrees. Combining this information with our $v \sin i$ value (Sect. 3) and $R_p/R_s = 0.08228$ (Gaudi et al. 2017), we calculated the expected RML effect RV curve. This theoretical curve, summed with the Keplerian orbital solution of Sect. 4, clearly does not match the in-transit RV time series (Fig. 4, right panel). Non-convective A-type stars like KELT-9 do not have spots. We thus investigated the possible reasons of the discrepancy between the observed RVs and the theoretical solution by looking at their differences (Fig. 5) and by analysing the tomography of the mean line profiles. This was created by dividing for each transit observed all the mean line profiles by a master out-of-transit mean line profile. All four transits were then combined to obtain Fig. 6.

The resulting RV residuals from the theoretical solution (Fig. 5) clearly show another RML-like shape. This is actually not surprising as in the tomography of the mean line profile residuals (Fig. 6) the planetary atmospheric track is evident, as it is in Gaudi et al. (2017) and Hoeijmakers et al. (2018, 2019) as well. We could thus expect this signal, given that the planetary RVs are within the width of the stellar mean line profile for the whole transit duration.

We performed an RML fit to these residuals, using the IDL routine MPFIT and the model of Ohta et al. (2005) as implemented in EXOFAST (Eastman et al. 2013), fixing the $v \sin i$ and the linear limb darkening to the values we estimated in Sect. 3. We also decided to keep the inclination angle λ fixed at the value of $-180°$. This choice reflects two facts. First the atmospheric planetary signal, that causes the deviation of the global in-transit stellar RVs, moves at a velocity corresponding to that of the planetary RV. Second, contrarily to what happens for the Doppler shadow which is associated with a relative flux increase (a positive "bump" moving along the mean line profile), it represents a further absorption. The planetary signal will thus cross the stellar mean line profile from negative to positive velocities, like in the case of the Doppler shadow of an aligned planet, but since it is giving a further absorption and not a reduction of it, the measured RV shift will have opposite sign. The effect on the RVs will thus be like that of a planet transiting with a projected obliquity of $-180°$. We note that any possible deviation from $-180°$ could be a hint of eccentricity of the planetary orbit. Our choice to impose the value of $-180°$ is thus also consistent with the circular orbital solution adopted. Leaving λ as a free parameter in the fit, however, does not change its full compatibility with the imposed $-180°$ value ($\lambda = -175 \pm 20$ degrees). The fit of this Atmospheric RML gives a value of $R_p/R_s = 0.058 \pm 0.004$. We interpret this as the R_{atmo}/R_s of the atmospheric layer that matches the stellar model used to extract the mean line profiles.

One way to detect the atmosphere of exoplanets using chromatic RVs was proposed by Snellen (2004), who analysed the amplitude of the RML effect at different wavelengths to retrieve a transmission spectrum. If the planetary apparent radius varies with wavelength, this will result in a different amplitude of the RML effect. Di Gloria et al. (2015) successfully applied the technique to high-resolution spectroscopic observations of HD 189733b, finding evidence of Rayleigh scattering in its atmosphere.

We made an attempt to see if any chromatic effect caused by the planetary atmosphere could be detected in our RV measurements of KELT-9. We split each spectrum into two parts, setting 5500 Å as the dividing value, and performed the same analysis again, as described in Sect. 3. No significant difference is found with the R_p/R_s from the Atmospheric RML fit. This is mainly due to the low S/N found in the stellar mean line profile of the redder half of the spectra, caused by the low number of stellar lines for such a spectral type.

As a second approach, we created stellar masks using only Ti, FeI, and FeII lines, respectively. The only case in which we reached sufficient RV precision to detect in-transit deviations from the Keplerian motion is with the FeII mask, for which the atmospheric RML effect results are fully compatible with those obtained using the complete A0 stellar mask. This is

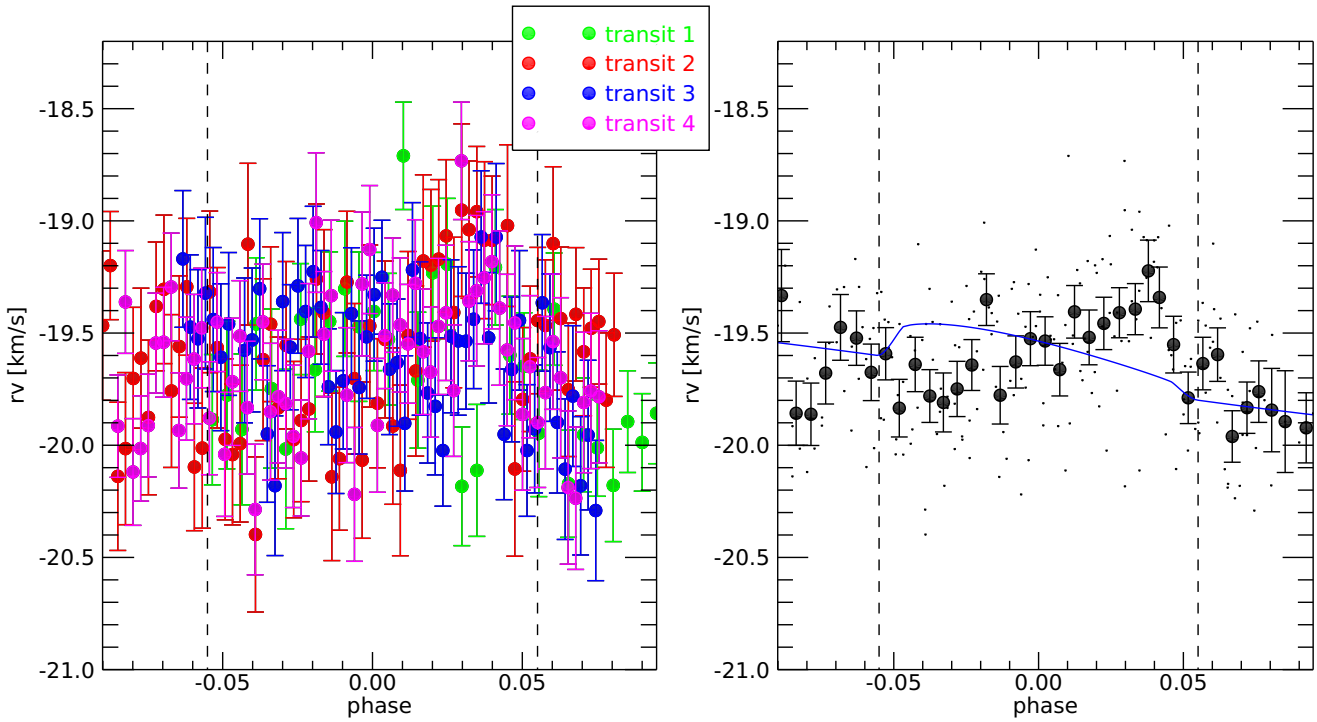

Fig. 4. *Left panel*: phase-folded RVs of the four HARPS-N transits of KELT-9b. Different colours refer to different transits. *Right panel*: mean RVs of the four transits (filled circles), together with single RVs (small dots). The theoretical RV solution (blue line) computed using Keplerian motion and the classical RML effect alone clearly does not match the observations. The vertical dashed lines show the ingress and egress of transit.

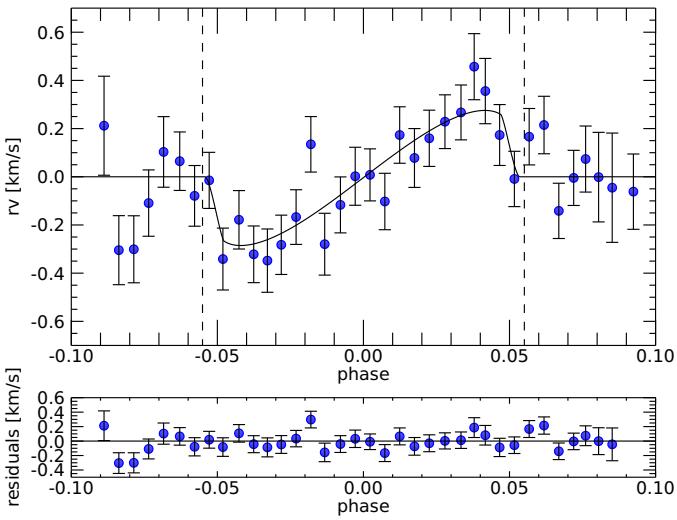

Fig. 5. Atmospheric RML effect of KELT-9b. The vertical dashed lines show the ingress and egress of transit.

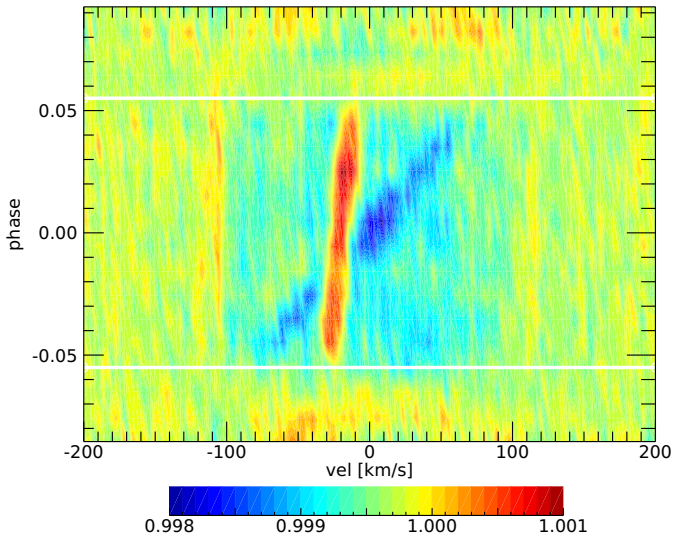

Fig. 6. Mean line profile residuals tomography of the four KELT-9 transits observed, centred in the stellar restframe. The horizontal white lines show the ingress and egress of transit. The doppler shadow of the planet (red) and the planetary atmosphere track (blue) are both evident. The depression during the transit (light blue) is caused by the photometric decrease of flux.

another confirmation of the strong presence of FeII in the atmosphere of KELT-9b, previously detected at >20σ significance (Hoeijmakers et al. 2018).

6. Discussion

The atmosphere of KELT-9b, with a dayside equilibrium temperature $T_{\rm eq} \sim 4000$ K, has been proven to host metals in a gaseous and excited state (Hoeijmakers et al. 2018). As a result, it significantly correlates with the stellar model that we used to retrieve the stellar mean line profile. This leaves an imprint in the stellar mean line profile during each transit at the corresponding RV of the planet and, as a consequence, affects the values of the retrieved RVs of the star.

We do not find any evidence of significant asymmetry in the atmospheric RML shape. It is interesting to note, however, that the phase where the residual RVs show the largest discrepancy from the fit (Fig. 5) is at approximately −0.02, which is the same phase where the two tracks of the Doppler shadow and planetary atmosphere intersect (Fig. 6). This deviation appears to happen for all the analysed transits (Fig. 4, left panel), so it looks unlikely

that it is just due to outliers. The deviation could be due to the partial cancellation that the Doppler shadow and the atmospheric track give to each other. Another possibility is that it is caused by the symmetric line profile adopted for fitting the LSD profiles, and thus for measuring the RVs (Winn et al. 2005; Triaud et al. 2009), and this effect is enhanced in the overlap of different asymmetries.

We hypothesise that the anomalous signal intercepted in our analysis of the stellar mean line profile is given only by the planetary atmosphere. Thus, the $R_{\rm atmo}/R_{\rm s}$ of the atmospheric RML fit refers to the atmosphere as if it were a disk, and we compare the area of this disk to the value of the planetary area extracted from photometric transits. We take as reference $R_{\rm p}/R_{\rm s} = 0.08228 \pm 0.00043$ (Gaudi et al. 2017). Comparing the two resulting areas, the atmospheric area represents ~51% of the photometric planetary area. We do not have any hint on the atmospheric shape, but if we hypothesise the most simple case of an atmosphere as an annulus surrounding the planetary core, this could translate to a $R_{\rm p+atmo} = 1.22 \pm 0.02\ R_{\rm p}$. Considering that Yan & Henning (2018) found a radius at the Hα line centre ~1.64 times the size of the planetary radius, this is another confirmation of an extended atmosphere and that also heavy atoms are present at rather high altitudes.

7. Conclusions

We extracted RVs of KELT-9 from HARPS-N spectra with an appropriate model to derive RVs for fast rotators, by using a rotational profile instead of a Gaussian to fit the stellar mean line profiles. This method led to more precise results. With the new set of spectra and RVs and by exploiting the *Gaia* DR2 we were able to update the orbital and physical parameters of the system.

We evidenced an in-transit RV deviation from the Keplerian orbital solution, which is not caused by the RML effect alone. This further deviation, which we call Atmospheric RML, is caused by the atmosphere of the transiting planet. The Atmospheric RML signal is obtained analogously to previous detections of the transmission spectra of exoplanets HD 209458 b (Snellen et al. 2010) and HD 189733 b (Brogi et al. 2016, 2018) with near-infrared high-resolution spectroscopy, with the important difference that in those studies the search for exoplanetary signals was performed with template spectra appropriate for the atmosphere of the planet, and the star was seen as a contaminating RML effect (e.g. Brogi et al. 2016), whereas in this case the planet signal is picked up with a mask optimised for the parent star. This is once again due to the exceptionally high planet temperature, which creates conditions more like a stellar photosphere than a classic planet atmosphere.

To our knowledge, this is the first time that such an effect has been observed in RVs. By analysing in detail this anomaly, we were able to determine the mean atmospheric height (as weighted with the stellar mask) of KELT-9b. We note that in particular cases of projected spin-orbit angle close to $\lambda = 0$, this effect could not be seen even if present. However, it could lead to an underestimation of $R_{\rm p}/R_{\rm s}$ and/or $v \sin i$ when fitting for the RML effect. In this case the planetary atmospheric track and the Doppler shadow can completely overlap if the excursion of the in-transit planetary RVs is $\sim 2 \times v \sin i$.

We also note that the duration of the Atmospheric RML coincides with that of the transit only when the in-transit planetary RVs are within the stellar mean line profile, as is the case for KELT-9. For other cases, depending on the $v \sin i$ of the star and on the orbital parameters of the system, this effect will only be present in the central phase of the transit when the planetary RVS fall within the stellar mean line profile range. This could lead to strange in-transit RV variations. The Atmospheric RML will be observable for other exoplanets whose atmospheres have a non-negligible correlation with the stellar mask used to retrieve the RVs, in particular ultra-hot Jupiters with iron in their atmospheres.

Acknowledgements. We thank the referee for the useful comments that helped improve the clarity of the paper. We acknowledge the support by INAF/Frontiera through the "Progetti Premiali" funding scheme of the Italian Ministry of Education, University, and Research. F.B. acknowledges financial support from INAF through the ASI-INAF contract 2015-019-R0. D.B. acknowledges financial support from INAF and the Agenzia Spaziale Italiana (ASI grant n. 014-025-R.1.2015) for the 2016 PhD fellowship programme of INAF. This work has made use of data from the European Space Agency (ESA) mission *Gaia* (https://www.cosmos.esa.int/gaia), processed by the *Gaia* Data Processing and Analysis Consortium (DPAC, https://www.cosmos.esa.int/web/gaia/dpac/consortium). Funding for the DPAC has been provided by national institutions, in particular the institutions participating in the *Gaia* Multilateral Agreement.

References

Anderson, D. R., Temple, L. Y., Nielsen, L. D., et al. 2018, MNRAS, submitted [arXiv:1809.04897]
Baranne, A., Queloz, D., Mayor, M., et al. 1996, A&AS, 119, 373
Bonomo, A. S., Desidera, S., Benatti, S., et al. 2017, A&A, 602, A107
Borsa, F., Scandariato, G., Rainer, M., et al. 2015, A&A, 578, A64
Brogi, M., de Kok, R. J., Albrecht, S., et al. 2016, ApJ, 817, 106
Brogi, M., Giacobbe, P., Guilluy, G., et al. 2018, A&A, 615, A16
Cauley, P. W., Shkolnik, E. L., Ilyin, I., et al. 2019, AJ, 157, 69
Claudi, R., Benatti, S., Carleo, I., et al. 2017, Eur. Phys. J. Plus, 132, 364
Collier Cameron, A., Bruce, V. A., Miller, G. R. M., et al. 2010, MNRAS, 403, 151
Covino, E., Esposito, M., Barbieri, M., et al. 2013, A&A, 554, A28
Deming, L. D., & Seager, S. 2017, J. Geophys. Res. Planets, 122, 53
Di Gloria, E., Snellen, I. A. G., & Albrecht, S. 2015, A&A, 580, A84
Donati, J.-F., Semel, M., Carter, B. D., Rees, D. E., & Collier Cameron, A. 1997, MNRAS, 291, 658
Dotter, A. 2016, ApJS, 222, 8
Eastman, J. 2017, Astrophysics Source Code Library [record ascl:1710.003]
Eastman, J., Gaudi, B. S., & Agol, E. 2013, PASP, 125, 923
Fossati, L., Bagnulo, S., Monier, R., et al. 2007, A&A, 476, 911
Fossati, L., Ryabchikova, T., Bagnulo, S., et al. 2009, A&A, 503, 945
Fossati, L., Koskinen, T., Lothringer, J. D., et al. 2018, ApJ, 868, L30
Gaia Collaboration (Prusti, T., et al.) 2016, A&A, 595, A1
Gaia Collaboration (Brown, A. G. A., et al.) 2018, A&A, 616, A1
Gaudi, B. S., Stassun, K. G., Collins, K. A., et al. 2017, Nature, 546, 514
Gray, D. F. 1976, Research Supported by the National Research Council of Canada (New York: Wiley-Interscience), 484
Gray, D. F. 2008, The Observation and Analysis of Stellar Photospheres (Cambridge, UK: Cambridge University Press)
Husser, T.-O., Wende-von Berg, S., Dreizler, S., et al. 2013, A&A, 553, A6
Hoeijmakers, H. J., Ehrenreich, D., Heng, K., et al. 2018, Nature, 560, 453
Hoeijmakers, H. J., Ehrenreich, D., Kitzmann, D., et al. 2019, A&A, 627, A165
Johnson, M. C., Rodriguez, J. E., Zhou, G., et al. 2018, AJ, 155, 100
Kitzmann, D., Heng, K., Rimmer, P. B., et al. 2018, ApJ, 863, 183
Kochukhov, O. 2007, Spectrum synthesis for magnetic, chemically stratified stellar atmospheres, Physics of Magnetic Stars, 109
Lothringer, J. D., Barman, T., & Koskinen, T. 2018, ApJ, 866, 27
Madhusudhan, N., Agúndez, M., Moses, J. I., & Hu, Y. 2016, Space Sci. Rev., 205, 285
Ohta, Y., Taruya, A., & Suto, Y. 2005, ApJ, 622, 1118
Parviainen, H., & Aigrain, S. 2015, MNRAS, 453, 3821
Pepe, F., Mayor, M., Galland, F., et al. 2002, A&A, 388, 632
Piskunov, N., Kupka, F., Ryabchikova, T. A., Weiss, W. W., & Jeffery, C. S. 1995, A&AS, 112, 525
Reiners, A., & Schmitt, J. H. M. M. 2002, A&A, 384, 155
Shulyak, D., Tsymbal, V., Ryabchikova, T., Stütz, C., & Weiss, W. W. 2004, A&A, 428, 993
Sing, D. K., Fortney, J. J., Nikolov, N., et al. 2016, Nature, 529, 59
Snellen, I. A. G. 2004, MNRAS, 353, L1
Snellen, I. A. G., de Kok, R. J., de Mooij, E. J. W., & Albrecht, S. 2010, Nature, 465, 1049
Stassun, K. G., & Torres, G. 2018, ApJ, 862, 61
Ter Braak, C. J. F. 2006, Stat. Comput., 16, 239

Triaud, A. H. M. J., Queloz, D., Bouchy, F., et al. 2009, A&A, 506, 377
Winn, J. N., & Fabrycky, D. C. 2015, ARA&A, 53, 409
Winn, J. N., Noyes, R. W., Holman, M. J., et al. 2005, ApJ, 631, 1215
Yan, F., & Henning, T. 2018, Nat. Astron., 2, 714

[1] INAF – Osservatorio Astronomico di Brera, Via E. Bianchi 46, 23807 Merate (LC), Italy
e-mail: francesco.borsa@inaf.it; francesco.borsa@brera.inaf.it
[2] INAF – Osservatorio Astrofisico di Arcetri, Largo E. Fermi 5, 50125 Firenze, Italy
[3] INAF – Osservatorio Astrofisico di Torino, Via Osservatorio 20, 10025, Pino Torinese, Italy
[4] Dipartimento di Fisica, Università degli Studi di Torino, Via Pietro Giuria 1, 10125 Torino, Italy
[5] Space Research Institute, Austrian Academy of Sciences, Schmiedlstrasse 6, 8042 Graz, Austria
[6] INAF – Osservatorio Astrofisico di Catania, Via S. Sofia 78, 95123, Catania, Italy
[7] INAF – Osservatorio Astronomico di Padova, Vicolo dell'Osservatorio 5, 35122 Padova, Italy
[8] Thüringer Landessternwarte Tautenburg, Sternwarte 5, 07778 Tautenburg, Germany
[9] INAF – Osservatorio Astronomico di Palermo, Piazza del Parlamento, 1, 90134 Palermo, Italy
[10] Fundación Galileo Galilei – INAF, Rambla José Ana Fernandez Pérez 7, 38712 Breña Baja, TF, Spain
[11] INAF – Osservatorio Astronomico di Trieste, Via Tiepolo 11, 34143 Trieste, Italy
[12] Department of Physics, University of Warwick, Coventry CV4 7AL, UK
[13] Centre for Exoplanets and Habitability, University of Warwick, Gibbet Hill Road, Coventry CV4 7AL, UK
[14] Astronomy Department, 96 Foss Hill Drive, Van Vleck Observatory 101, Wesleyan University, Middletown, CT 06459, USA
[15] INAF – Osservatorio Astronomico di Capodimonte, Salita Moiariello 16, 80131 Napoli, Italy
[16] Dipartimento di Fisica e Chimica Emilio Segré – Università di Palermo, Piazza del Parlamento, 1, 90134 Palermo, Italy
[17] Centro de Astrobiología (CSIC-INTA), Carretera de Ajalvir km 4 - 28850 Torrejón de Ardoz, Madrid, Spain
[18] Department of Physics, University of Rome Tor Vergata, Via della Ricerca Scientifica 1, 00133 Rome, Italy
[19] Max Planck Institute for Astronomy, Königstuhl 17, 69117 Heidelberg, Germany
[20] INAF – Osservatorio di Cagliari, Via della Scienza 5, 09047 Selargius, CA, Italy
[21] Dipartimento di Fisica e Astronomia Galileo Galilei – Università di Padova, Vicolo dell'Osservatorio 2, 35122 Padova, Italy
[22] Anton Pannekoek Institute for Astronomy, University of Amsterdam, Science Park 904, 1098 XH Amsterdam, The Netherlands
[23] INAF – Osservatorio Astronomico di Roma, Via Frascati 33, 00078 Monte Porzio Catone, Italy
[24] Fondazione GAL Hassin, Via della Fontana Mitri, 90010 Isnello (PA), Italy